Schnubel, D.; Horstmann, M.; Ventzke, V.; Riekehr, S.; Staron, P.;
Fischer, T.; Huber, N.:

Retardation of fatigue crack growth in aircraft aluminium alloys via laser heating - Experimental proof of concept

In: Materials Science and Engineering A (2012) Elsevier

DOI: 10.1016/j.msea.2012.02.094

Retardation of fatigue crack growth in aircraft aluminium alloys via laser heating - Experimental proof of concept

D. Schnubel[a,*], M. Horstmann[a], V. Ventzke[a], S. Riekehr[a], P. Staron[b], T. Fischer[b], N. Huber[a]

[a] *Institute of Materials Research, Materials Mechanics, Helmholtz-Zentrum Geesthacht, 21502 Geesthacht, Germany*
[b] *Institute of Materials Research, Materials Physics, Helmholtz-Zentrum Geesthacht, 21502 Geesthacht, Germany*

Abstract

In this work, a defocused laser was used to modify the residual stress state in AA2198-T8 C(T)100 specimens with the goal of retarding fatigue crack growth. The manuscript provides a description of the process, the resulting changes of the material properties and the modified fatigue crack growth behaviour. The performed experiments, including thermocouple measurements, microscopical examinations, micro-hardness measurements, residual stress measurements and fatigue crack growth measurements under constant amplitude loading show, that via laser heating a substantial retardation of fatigue crack growth can be achieved.

Keywords: Laser heating, Aluminium alloys, Synchrotron X-ray diffraction, Residual stresses, Fatigue crack growth

*Corresponding author
Email address: dirk.schnubel@hzg.de, Phone: +49 4152 87-2637 (D. Schnubel)
URL: http://www.hzg.de, Fax: +49 4152 87-2549 (D. Schnubel)

Nomenclature

E	Young's modulus
$F_{\max}$	Maximum applied load
K	Stress intensity factor
N	Number of load cycles
R	Stress intensity ratio or load ration
T	Temperature
BM	Base material or zone with base material properties
HZ	Heating zone
HAZ	Heat affected zone
$\mathrm{d}a/\mathrm{d}N$	Fatigue crack growth rate
ν	Poisson's ratio
ϵ	Elastic strain
σ_{xx}	Transverse stress component
σ_{yy}	Longitudinal stress component
$\Delta\ \sigma$	Stress difference σ_{yy}-σ_{xx}
a	Crack length
a_0	Initial notch length
d_0	Stress free lattice parameter
t	Time
x, y, z, θ	Coordinates

1. Introduction

The modification of the residual stress state in structures to improve their mechanical performance is a commonly used method. However, especially for safety-critical applications, such as airframe structures, a detailed review of the different aspects and problems is necessary, which can arise when utilising residual stresses based life enhancement techniques.

The work published by McClung [1] gives an informative and detailed overview of this specific topic. The key points are summarised as follows. The utilisation of residual stress modifications to extend the fatigue life of aerospace structures raises a dilemma for operators and regulators. Residual stresses can have notably beneficial effects on fatigue performance. However, after production, it is nearly impossible to measure the actual amount of induced residual stresses and there exists the possibility of changes of the initial residual stress state e.g. due to applied service loads [1] or the changing service temperatures [2]. Besides, residual stress effects are normally not addressed by the methodologies commonly used for life prediction and damage tolerance evaluation[3]. For this reasons regulation authorities normally claim that damage tolerance requirements have to be reached without considering potential positive residual stress effects in the design.

Nevertheless, even without official credit the manufacturers and operators continue to use residual stress based life enhancement techniques, because experience has shown that they are effective and their use helps reducing the maintenance costs. For this reason these stress based methods are also believed to offer a cost-efficient way to significantly extend the service life of ageing aircraft [1]. Based on its substantial economic potential, this consideration is a strong motivation for manufacturers and operators to further improve established and investigate new stress based techniques for life enhancement.

The underlying principle of all processes that aim to improve fatigue performance by changing the residual stress state is the same. This principle is the induction of local, non-uniform plastic yielding to create compressive residual stresses at critical positions, which decrease the total stress intensity under application loads. Because a broad variety of work has been published during the last years examining such methods as shot peening, laser shock peening or cold expansion, these processes will not be discussed here. Instead, a brief review of the performed studies using local heating with and without additional mechanical loading for the well-directed introduction of residual stresses is be presented because this subject forms the basis of the presented work.

In an early work published by Gurney [4], local spot heating was used as a life extension and repair technique. Spot heating was applied to generate different stress states at the run-in and run-out positions of double-fillet welded mild-steel specimens. Significant improvement of the S-N behaviour was obtained. By comparing these results to those of specimens that were subjected to local mechanical pressing with a punch that clearly produced compressive stresses at the critical positions, it was concluded that the observed effect in the heated specimens was mainly due to residual stresses. This work was later extended

one step further by Harrison [5]. In this work, the spot heating technique was used to repair fatigue specimens on which premature cracking was observed in the run-in of some welds. It was shown that by applying spot heating the fatigue life of specimens could be extended significantly.

Verma and Ray [6–8] performed some mainly experimentally based work comparing the observed retardation effects of the fatigue crack growth rates in steel specimens after spot heating to the ones observed after single overloads. They examined the impact of process parameters like spot heating position or heating temperature and concluded that the effects of spot heating and of single mechanical overloads can be compared in general. However, the underlying physical effects were not further investigated.

Several authors combined the heating and mechanical loading of cracked specimens and components [9–14]. However, the aim of the proposed procedures was not a direct generation of thermally induced residual stresses. The heating was only applied to promote plastic yielding under an applied load at the crack tip by lowering the yield stress. This approach showed notably promising results. For one case [12], it was even possible to completely arrest a crack in a mild steel plate with an applied stress intensity $K_{\mathrm{appl}} = 20\mathrm{MPa}\sqrt{\mathrm{m}}$. However, this method is only applicable to specimens or structures already containing cracks or sharp notches and where mechanical loading is easy to perform. If these two conditions are met, it can be a suitable method for fatigue life extension, as demonstrated for the case of aluminium gas cylinders in [13].

In the work presented by Tsay et al. [15–18] a laser was used to create heating lines on C(T) specimens composed of stainless steel. Afterwards, fatigue crack growth tests were performed. It was concluded that the observed retardation effects were caused by the heating-induced residual stresses because the effect ceased after a stress-relieving heat treatment.

In the presented work, a defocused laser was used to create heating lines on aluminium C(T) specimens with the goal of modifying the residual stress state in a manner that leads to the retardation of the measured fatigue crack growth. Experiments were performed on specimens containing one line of laser heating in comparison to base material specimens that were not subjected to laser heating. The results presented in this study are an experimental proof of this principle for aluminium specimens.

2. Material and Experiments

2.1. Material and specimen preparation

The latest generation of Al-Li alloys was developed in the 1990s. Compared to previous alloys, these alloys show an improved ductility and fracture toughness, due to a reduction of the Li content ($<$ 2.0 wt.% Li). In these alloys, the main strengthening phase was T_1 (Al_2CuLi). Such alloys as 2195, 2x96, 2x97 and 2098 had commercial applications mostly in the USA. These alloys were able to match the balance between the strength and damage tolerance of standard aircraft alloys, such as 2024 or 7050 [19]. However, recent metallic airframes use more advanced high strength and high damage tolerant alloys. For

this reason, the Al-Cu-Mg-Li alloy 2198 was developed by Alcan (since 2011 Constellium) as new aircraft skin material with the goal of reaching a higher static strength than AA7475 and to have better damage tolerance capabilities than AA2524 [19, 20]. The alloy 2198 is a derivative of AA2098 with a lower copper content, several other minor chemistry adoptions and optimised thermo-mechanical processing [20]. Additionally, AA2198 is weldable via laser beam welding and friction stir welding [19–21]. Thermo-mechanical treatment during production leads to a microstructure consisting of flat, pancake-like grains lying in the L-T plane, which leads to a pronounced anisotropy of the mechanical properties [22].

2.2. Specimen preparation

A batch of C(T)100 specimens in the L-T orientation with a notch length $a_0 = 20$ mm and rectangular pieces with a size of 125 mm x 120 mm were produced from a sheet of AA2198 in T3 temper with a nominal thickness of 5 mm. Afterward, heat treatment to reach T8 temper was conducted. The dimensions of the C(T)100 specimens were in accordance with ASTM E647 [23], as shown in Fig. 1a. However, the thickness of only 5 mm is lower than the standard requirements but is common for thin sheet testing. During the fatigue crack growth experiments, the majority of the tested specimens unfortunately showed such severe deviations of the crack path that a clear evaluation of the results according to ASTM-E647 [23] could not be obtained. Therefore, a second batch of specimens with the same dimensions but in the T-L orientation was prepared from the same AA2198 sheet as used before, and the fatigue crack growth tests were repeated. Even though some crack deviation could be also observed for this second series of tests, it was much less pronounced than in the first series of tests. The results from the T-L orientation tests are presented in the following sections.

2.3. Laser Heating

For the performed experiments, a Nd:YAG laser was used to produce a line of laser heating on the surface of the prepared C(T)100 specimens. For this, the laser was moved with a travelling speed of 3.33 mm/s in positive y-direction from one edge of the specimen to the other. Figure 1 shows a sketch and a photograph of one of the specimens after the treatment. The heating line was positioned at $x_{heating} = 55$ mm for all specimens. Because the goal was to apply heat without localized melting of the material, a welding optic was used, but the working distance was increased to achieve a laser spot diameter of approximately 5 mm. A layer of silicon carbide powder with a thickness of 0.5 mm was placed on the irradiated surface to ensure the equal absorption of the laser light for all specimens. After the treatment, a slight out-of-plane distortion of the specimens in the range of approximately 1 mm could be observed. As shown in Fig. 1b, along the heating line, a slight colour change on the surface with a slight roughness increase was observed, but no signs of melting were found.

The same process parameters set was used for the laser heating of all specimens.

2.4. Thermocouple measurements

The transient temperature distribution during laser heating was characterised using 12 type K thermocouples. The thermocouples were placed in prepared rectangular pieces of AA2198 T8 with outer dimensions of C(T)100 specimens. Table 1 provides the exact positioning of the thermocouples. The thermocouples were placed in holes drilled to a depth of half the specimen's thickness from the far side of the laser heating, as indicated in Fig. 1a. For data acquisition, a computer-based measurement system with a sampling rate of 400 Hz was used.

2.5. Microscopical examinations and micro-hardness measurements

The resulting micro structure after laser heating was studied using a light optical microscope (OM). Additionally, a scanning electron microscope (SEM) in conjunction with the electron backscatter diffraction (EBSD) technique was used to study changes in the grain structure. Changes in the local mechanical properties due to the laser heating were measured via micro-hardness measurements. For each indent with the pyramidal diamond tip, a load of 0.2 kp with a hold time of 20 s was used.

2.6. Residual stress measurements

Prior to the residual stress measurements, a fatigue crack with a length of $a = 30$ mm was grown in the examined laser heated specimen under the same loading conditions that were later used for the fatigue crack-growth experiments. The residual stress measurements were performed at the HARWI II beamline of HZG at the synchrotron source DORIS III at DESY. The sychrotron diffraction experiments were performed at a photon energy of 70 keV and with a beam cross-section of 1 mm x 1 mm. A Mar555 area detector was used to record several complete diffraction rings. Approximately 1000 single pictures were recorded for a scan of the area in front of the crack tip. Copper paste was placed on one side of the specimen and covered the entire scan area marked in Fig. 1a.

For the evaluation of the detector data, a python routine was written that allows the use of the information of the complete Al-311 ring for the calculations. As a first step in the evaluation, the detector data were transformed from cartesian coordinates (x,y) into polar coordinates (r,θ). Then, the data were divided into 720 small sectors, with each representing one individual direction θ. As the next step, the shift of the Al-311 peak and the resulting elastic strain in the corresponding θ-direction $\epsilon'(\theta)$ were calculated for each sector. To suppress the effects of specimen distortion or misalignment, during the performed calculations, the absolute peak shift of the Al-311 peaks was not used; instead, the relative shift in comparison to the neighbouring copper peak was used. In the final step, an optimisation algorithm was used to obtain the best fit for

the global strains ϵ_{xx}, ϵ_{yy} and ϵ_{xy} using the 720 individually calculated $\epsilon'(\theta)$ in Equation (1):

$$\epsilon'(\theta) = \epsilon_{xx}\cos^2(\theta) + \epsilon_{xy}\sin(2\theta) + \epsilon_{yy}\sin^2(\theta) \quad (1)$$

For the following calculations of the resulting stresses, a Young's Modulus $E = 70$ GPa and a Poisson's ratio $\nu = 0.35$ were assumed. The stress-free lattice parameter was manually adjusted to $d_0 = 1.217$ $\mathring{A}$ in a manner such that the transverse residual stresses σ_{xx} became zero at the specimen edge ($x = 100$ mm).

Because heating leads to a change in the precipitation state, as discussed subsequently, it can be expected that this also causes a local variation of the stress-free lattice parameter d_0 in the heating zone (HZ) and the heat affected zone (HAZ). Because this effect was neglected during the evaluation, the entire presented discussion is based on the difference of the mean stresses components $\Delta\ \sigma = \sigma_{yy} - \sigma_{xx}$, which is rather insensitive to changes in the d_0. As known from measurement results for aluminium welds [24, 25], the transverse residual stresses σ_{xx} are expected to be very small. This finding means that the stress difference $\Delta\ \sigma = \sigma_{yy} - \sigma_{xx}$ represents mainly the state of the longitudinal residual stress component σ_{yy}.

The results obtained after the evaluation of the raw data represent averaged values for the stresses in the gauge volume of 1 mm x 1 mm x 5 mm. Therefore stress gradients through the thickness of the specimens (z-direction) cannot be decomposed, but the measured stress values give an average throughout the specimen's thickness.

2.7. Fatigue crack growth tests

The force-controlled fatigue crack growth experiments were performed under constant amplitude loading conditions ($F_{max} = 4.41 \pm 0.015$ kN, $R = 0.1$) using a servo hydraulic testing machine. The crack length was monitored directly via optical measurements and indirectly via a clip gauge spanned over the notch that recorded the opening of the notch faces. On the basis of the optical crack length measurement results, a polynomial fitting function was established to convert the clip data into crack length data. For more details on the set-up that was used, see [26].

To calculate the crack growth rates, the incremental polynomial method, as recommended in ASTM E647 Appendix X1.2 [23] with a fitting half window size $n = 4$, was used. To suppress any effect of fatigue crack initiation at the initial notch tip ($a_0 = 20$ mm), the number of loading cycles was reset to zero in the evaluation for all specimens after the crack reached a length of $a = 25$ mm.

3. Results

The specimen names begin with a prefix BM for base material or LH for laser heated specimens, which is followed by a suffix consisting of a code for the performed experiment (thermo couple measurement (TC), macro cross section (CS), micro hardness measurements (MH), residual stress measurements (RS)

or fatigue crack growth test (FCG)), and, where required, a specimen number and/or a further specification of the measurement position is given.

3.1. Temperature field measurements

Figure 2 shows the results of the performed thermocouple measurements. As shown in Fig. 2b, the T_{max} distribution was rather symmetrical around the centre of the heating zone (HZ) at $x_{heating} = 55$ mm, where it reached a maximum of approximately 380 °C. Only one of the thermocouples at $x = x_{\text{heating}} = 55$ mm showed a significant lower T_{max} compared to the other three at the same x-position. This finding is assumed to be a measurement error due to a loss of thermal contact between the specimen and the thermocouple in the drilled hole.

In general, the results of the two individual measurements LH-TC-1 and LH-TC-2 lay nearly on top of each other, which indicates good reproducibility of the measurement set-up and the process.

3.2. Microscopical examinations and micro-hardness measurements

Figure 3 shows a light optical microscope picture of the laser heating area cut from the specimen LH-CS. The horizontal features in the picture are caused by the highly elongated grains in the $x - direction$. No significant changes in the micro-structure or signs of melting were found. Only beneath the laser irradiated surface area, which is indicated by the white arrows, a slight colour change is visible in a semi-elliptical area.

Figure 4 shows two SEM pictures of the grain structure in the same specimen using the EBSD technique. In Fig. 4a, the grain structure for the base material (BM) far away from the heating zone is shown. This structure consists of layers of elongated grains in the $x - direction$. Figure 4b shows a corresponding area directly from the heating zone (HZ). Additionally, many small grains in between the large elongated ones were found here.

Figure 5a shows a false colour plot of the results of a micro-hardness area scan performed on the specimen LH-MH. A significant reduction in the micro-hardness was found in the area beneath the laser irradiated surface. Figure 5b shows the results for $z = 1.8$ mm as a line plot. The dark shaded area indicates the lateral extension of the heating zone (HZ) with 52.5 mm $< x <$ 57.5 mm. The hardness drop is limited to the heat-affected zone (HAZ) with 45.0 mm $< x <$ 65.0 mm, which is marked as lightly shaded in Fig. 5b. The remaining part of the specimens shows the hardness of the base material (BM).

3.3. Residual stress measurements

Figure 6 shows the difference of the mean stress components $\Delta\sigma = \sigma_{yy} - \sigma_{xx}$ for the specimen LH-RS-1. As explained previously, $\Delta\sigma$ is dominated by the changes of the longitudinal residual stresses σ_{yy}.

Figure 6b shows the results as a line scan by averaging the corresponding data over y in the bounds of -12 mm to 12 mm for each position x. High positive values of $\Delta\sigma$ were found in the HZ and HAZ, which indicated high

tensile longitudinal residual stresses σ_{yy}. In the surrounding areas, moderate negative values of $\Delta\sigma$ were seen, indicating compressive longitudinal residual stresses σ_{yy}.

A value of $\Delta\sigma \approx -30$ MPa was found for 30 mm $< x <$ 47 mm. The values of $\Delta\sigma$ increased from $x = 47$ mm onwards, changed sign at $x = 49$ mm and reached a maximum plateau of 130 MPa between 52 mm $< x <$ 57 mm, corresponding approximately to the lateral extension of the HZ. With increasing x-position the values of $\Delta\sigma$ dropped again, changed sign to negative values at $x = 60$ mm and reached an almost constant level of $\Delta\sigma \approx -30$ MPa again for $x \geq 62$ mm.

3.4. Fatigue crack growth tests

As previously mentioned, all of the force-controlled tests were conducted with the same $R = 0.1$ and a constant $F_{max} = 4.41$ kN. Figure 7 shows the crack length a as a function of the loading cycles N. The crack growth of the two tested base material specimens (BM) is shown as diamond markers. Compared to the behaviour of the base material specimens, the crack growth in the laser-heated (LH) specimens was substantially slower, as can be seen from the high number of cycles required to reach the final crack length (circle markers).

Figure 8 presents the crack growth rates calculated on basis of the data shown in Fig. 7. For the base material specimens, a nearly linear dependence between crack growth rate and crack length was found in the semi-logarithmic plot. For the laser-heated specimens, a nearly constant shift downwards on the da/dN-axis was seen until the crack growth rates began to increase at $a = 48$ mm and nearly reached the same values as for the base material specimens at $a = 58$ mm.

Table 2 contains the measured maximum crack deviations for the tested specimens that all lay within the validity threshold of 20° defined in ASTM E647 [23].

4. Discussion

As indicated by the microscopical examinations, a small effect of the laser heating on the grain structure was found. The formation of small grains in the HZ indicates that in this area, a thermally activated partial recrystallisation took place. No signs of partial melting or surface crack formation were found.

The micro-hardness measurements indicate a clear change of the mechanical properties in the area of the HAZ and the HZ. In this area, the hardness decreases from the base material value of approximately 155 HV 0.2 kp to approximately 100 HV 0.2 kp. The observed severe changes of the hardness are not likely to be the result of the observed changes in the grain structure. The performed thermocouple measurements showed that in the HAZ and the HZ, peak temperatures of 225 °C $< T_{max} <$ 380 °C have been reached. These temperatures are well above the tempering temperatures that are used for this material in order to gain peak age after several hours. This finding suggests that the excessive heating in HAZ and HZ most likely changed the precipitation state there substantially, which explains the measured decrease of the hardness in these areas.

Although, in the HAZ and the HZ, an effect of the changed microstructure on the fatigue crack growth cannot be excluded, the observed crack growth retardation for $a < 45$ mm is clearly a result of the residual stresses alone. In this area, the measured residual stress differences $\Delta\sigma$ indicate the presence of compressive longitudinal residual stresses σ_{yy}. Because these compressive residual stresses act in parallel to the external applied load F, their main effect is a reduction of the total stress intensity factor K_{tot} at the crack tip, which is due to the combination of the applied load and the residual stresses.

With an increasing amplitude of the compressive stresses acting on the crack faces, the three following cases must be distinguished:

- The crack faces at the crack tip are completely open during the fatigue cycle. The compressive residual stresses only lower the stress intensity ratio, $R_{\mathrm{appl}} > R_{\mathrm{tot}} > 0$. Because the crack growth rate is rather insensitive to the stress ratio, this condition only leads to a small retardation of the crack growth.

- The crack faces at the crack tip are open under a maximum applied load but are closed under a minimum applied load. This condition leads to a decrease of the total stress intensity factor range $\Delta K_{\mathrm{appl}} > \Delta K_{\mathrm{tot}}$ and to a total stress intensity factor ratio of zero $R_{\mathrm{appl}} > R_{\mathrm{tot}} = 0$. Because the crack growth rate is notably sensitive to the stress intensity factor range, this condition can create such a large crack growth retardation effect as seen in Fig. 8.

- The crack faces at the crack tip are completely closed, even under a maximum applied load. This condition would lead to $\Delta K_{\mathrm{tot}} = R_{tot} = 0$. In this case, no further crack growth would occur.

A comprehensive presentation of the underlying mechanisms was published in [27], in which the prediction of crack growth rates for a crack growing through a residual stress field like the one shown in Fig. 6 was discussed.

5. Conclusion

The presented results give an experimental proof of the concept that it is possible to retard the fatigue crack growth effectively in aluminium C(T)100 specimens via laser heating. The lifetime of the laser heated specimens could be increased to approximately 300% of that one of the base material specimens.

At the same time, the heating led to a decrease in the hardness in the HZ and the HAZ. This fact raises concerns regarding the impact of laser heating on static strength when applied to lightweight structures. This point should be addressed in future research.

As can be expected, the obtained residual stress distribution after laser heating was found to be similar to that found after welding, with high tensile longitudinal residual stress being observed in the HZ, which were balanced by compressive longitudinal residual stresses in the surrounding areas. It can be

concluded that the observed fatigue crack growth retardation is most likely to be a purely residual stress effect, even though a possible minor effect of the altered micro-structure for HAZ and HZ cannot be completely excluded.

Acknowledgments

The authors wish to thank Dr. Waman Vishwanath Vaidya of Helmholtz-Zentrum Geesthacht, Germany for engaging in valuable discussions on this topic.

[1] R. C. McClung, A literature survey on the stability and significance of residual stresses during fatigue, Fatigue & Fracture of Engineering Materials & Structures 30 (2007) 173–205.

[2] R. H. Oskouei, R. N. Ibrahim, The effect of typical flight temperatures on the fatigue behaviour of Al 7075-T6 clamped plates, Materials Science and Engineering A 528 (2011) 1527–1533.

[3] D. Ball, The influence of residual stress on the design of aircraft primary structure, Journal of ASTM International 5 (2009) 216–239.

[4] T. Gurney, Influence of residual stresses on fatigue strength of plates with fillet welded attachments, British Welding Journal 7 (1960) 415–431.

[5] J. Harrison, Exploraty fattigue tests on local heating as repair technique, British Welding Journal 12 (1965) 258–260.

[6] B. B. Verma, P. K. Ray, Fatigue crack growth retardation in spot heated mild steel sheet, Bull. Mater. Sci. 25 (2002) 301–307.

[7] P. K. Ray, B. B. Verma, P. K. Mohanthy, Spot heating induced fatigue crack growth retardation, International Journal of Pressure Vessels and Piping 79 (2002) 373–376.

[8] P. K. Ray, P. K. Ray, B. B. Verma, A study on spot heating induced fatigue crack growth retardation, Fatigue & Fracture of Engineering Materials & Structures 28 (2005) 579–585.

[9] Y. C. Lam, J. R. Griffiths, The effect of intermittent heating on fatigue crack growth, Theoretical and Applied Fracture Mechanics 14 (1990) 37–41.

[10] G. K. Cole, Y. C. Lam, Fatigue life enhancement of specimens with stress concentrators using a thermo-mechanical technique, Scripta Metallurgica et Materialia 25 (1991) 2849–2853.

[11] Y. C. Lam, G. K. Cole, Fatigue life enhancement of butt welds using a thermo-mechanical technique, Fatigue and Fracture of Engineering Materials and Structures 16 (1993) 983–994.

[12] B. D. Chen, J. R. Griffiths, Y. C. Lam, The effects of simultaneous overload and spot heating on crack growth retardation in fatigue, Engineering Fracture Mechanics 44 (1993) 567–572.

[13] R. N. Ibrahim, R. S. D. Sayers, D. Ischenko, Retardation of crack growth in an aluminium alloy using a thermomechanical conditioning cycle, Engineering Fracture Mechanics 59 (1998) 215–224.

[14] R. K. S. Raman, R. N. Ibrahim, F. Wu, R. Rihan, Thermomechanical manipulation of crack-tip stress field for resistance to stress corrosion crack propagation, Metallurgical and Materials Transactions A 39 (2008) 3217–3223.

[15] L. W. Tsay, Y. C. Liu, D. Y. Lin, M. C. Young, The use of laser surface-annealed treatment to retard fatigue crack growth of austenitic stainless steel, Materials Science and Engineering A 384 (2004) 177–183.

[16] L. W. Tsay, M. C. Young, F. Y. Chou, R. K. Shiue, The effect of residual thermal stresses on the fatigue crack growth of laser-annealed 304 stainless steels, Materials Chemistry and Physics 88 (2004) 348–352.

[17] R. K. Shiue, C. T. Chang, M. C. Young, L. W. Tsay, The effect of residual thermal stresses on the fatigue crack growth of laser-surface-annealed AISI 304 stainless steel part I: computer simulation, Materials Science and Engineering A 364 (2004) 101–108.

[18] L. W. Tsay, T. Y. Yang, M. C. Young, Embrittlement of laser surface-annealed 17-4 PH stainless steel, Materials Science and Engineering A 311 (2001) 64–73.

[19] P. Lequeu, F. Eberl, S. Jambu, T. Warner, A. Danielou, B. Bes, Latest generation of Al-Li alloys developed by Alcan Aerospace, in: Proceedings of the 1st EUCOMAS European Conference on Materials and Structures in Aerospace, VDI Verlag, 2008, pp. 1–8.

[20] M. Knüwer, J. Schumacher, H. Ribes, F. Eberl, B. Bes, 2198 - Advanced Aluminium-Lithium Alloy for A350 Skin Sheet Application, in: Presentation for the 17th AeroMat Conference & Exposition, Seattle, USA, pp. 1–27.

[21] P. Lequeu, F. Eberl, S. Jambu, T. Warner, A. Danielou, B. Bes, Latest generation of Al-Li alloys developed by Alcan Aerospace, in: Presentation for the 19th AeroMat Conference & Exposition, Austin, Texas USA, pp. 1–24.

[22] J. Chen, Y. Madi, T. F. Morgeneyer, J. Besson, Plastic flow and ductile rupture of a 2198 Al-Cu-Li aluminum alloy, Computational Materials Science 50 (2011) 1365–1371.

[23] ASTM E647-05 Standard test method for measurement of fatigue crack growth rates, 2005.

[24] P. Staron, M. Koçak, S. Williams, Residual stress distributions in friction stir welded Al sheets determined by neutron strain scanning, in: 6th International Trends in Welding Research Conference Proceedings, pp. 253–256.

[25] P. Staron, W. Vaidya, M. Koçak, Precipitates in laser beam welded aluminium alloy AA6056 butt joints studied by small-angle neutron scattering, Materials Science and Engineering: A 525 (2009) 192–199.

[26] W. V. Vaidya, M. Horstmann, K. Angamuthu, M. Koçak, Parametric (Non)-Variance of the Mid-Regime Fatigue Crack Propagation in an Aluminium Alloy AA6056-T6, MP Materials Testing 52 (2010) 300–305.

[27] D. Schnubel, N. Huber, The influence of crack face contact on the prediction of fatigue crack propagation in residual stress fields, Engineering Fracture Mechanics (2012) doi:10.1016/j.engfracmech.2011.12.008.

Table 1: Thermocouple positions

TC Name	x [mm]	y [mm]	z [mm]
TC-1	55.00	9.00	0.00
TC-2	53.75	9.00	0.00
TC-3	50.00	9.00	0.00
TC-4	45.00	9.00	0.00
TC-5	35.00	9.00	0.00
TC-6	80.00	0.00	0.00
TC-7	75.00	0.00	0.00
TC-8	70.00	0.00	0.00
TC-9	65.00	0.00	0.00
TC-10	60.00	0.00	0.00
TC-11	56.25	0.00	0.00
TC-12	55.00	0.00	0.00

Table 2: Measured specimen thickness and maximum crack deviation.

Specimen	Thickness $[mm]$	Crack Deviation $[^\circ]$
BM-FCG-2	5.07	11.3
BM-FCG-3	5.07	3.1
LH-FCG-2	5.07	11.4
LH-FCG-3	5.07	7.3

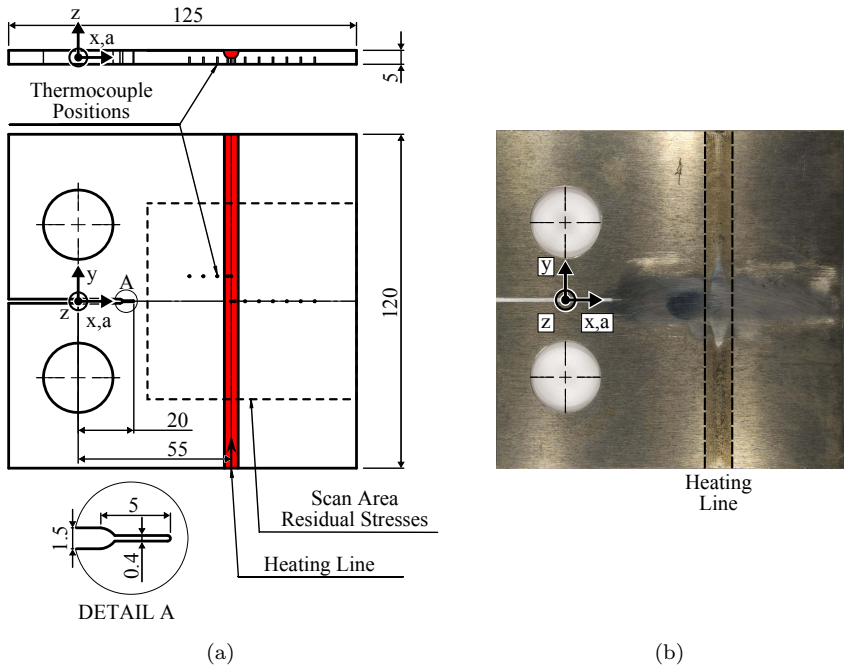

(a) (b)

Figure 1: (a) Sketch of the C(T)100 specimen geometry with the corresponding coordinate definitions. The origin of the z-coordinate is located at the middle of the specimen thickness and all measures given are in millimetres. (b) Picture of a laser-heated AA2198 T8 C(T)100 specimen before fatigue testing. The specimen surface along the expected crack path was manually polished for the optical crack-length measurements.

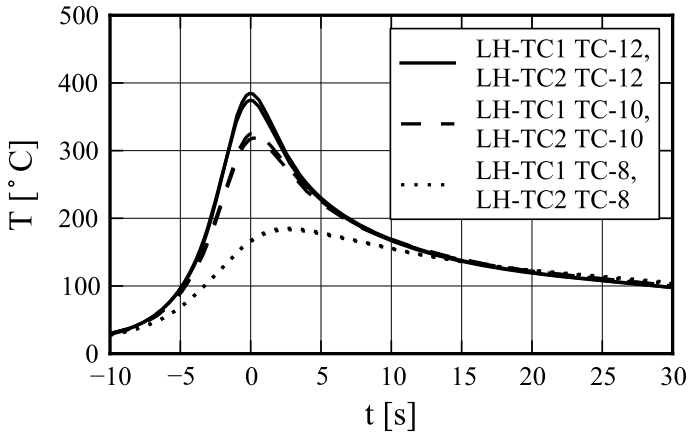

(a)

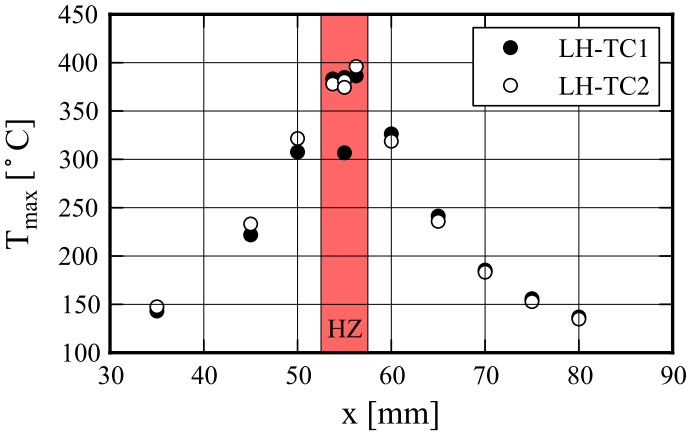

(b)

Figure 2: Thermocouple measurements results for the two specimens LH-TC1 and LH-TC2 (a) Measured temperature cycles for three of the thermocouple positions given in Table 1 and (b) Extracted maximum temperature $T_{\max}$ as a function of the x-position. The dark shaded area indicates the lateral extension of the heating zone (HZ) that corresponds to the spot diameter of the defocused laser.

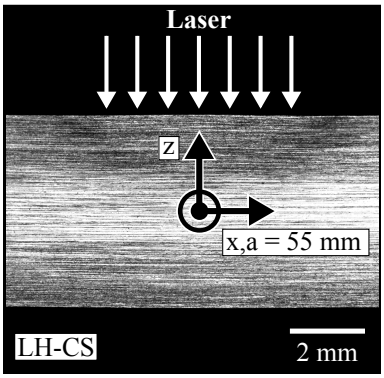

Figure 3: Light optical macrograph cross-section (x-z plane) of the specimen LH-CS at the indicated heating line centre position $x_{heating} = 55$ mm.

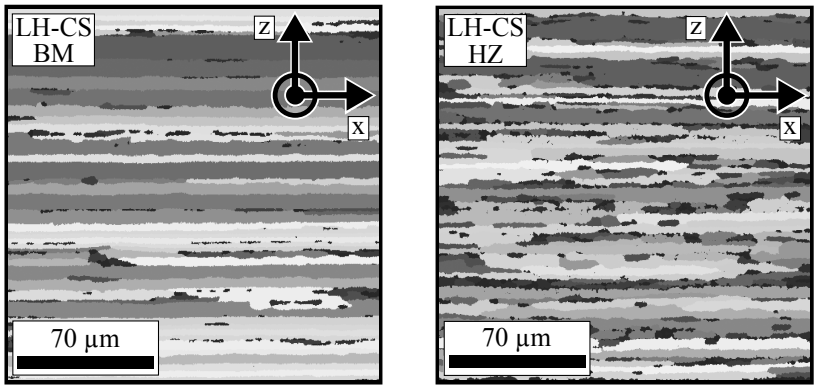

(a) (b)

Figure 4: Colour coded EBSD pictures of the grain structure of the specimen LH-CS after laser heating: (a) position distant from the heating zone and (b) in the heating zone directly under the laser heated specimen surface ($z = 2.0$ mm). Different grey values indicate different grains.

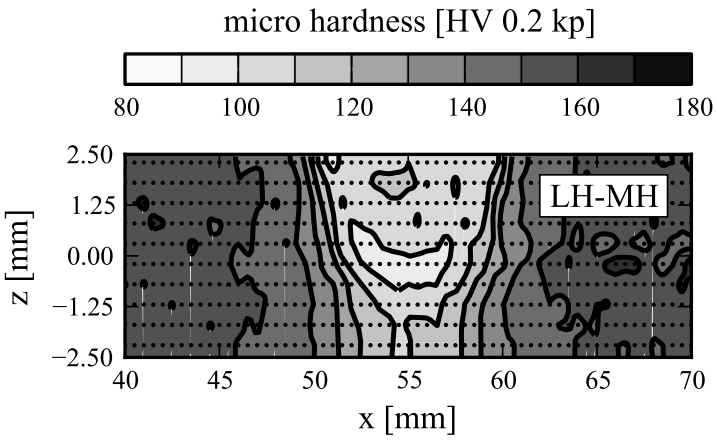

(a)

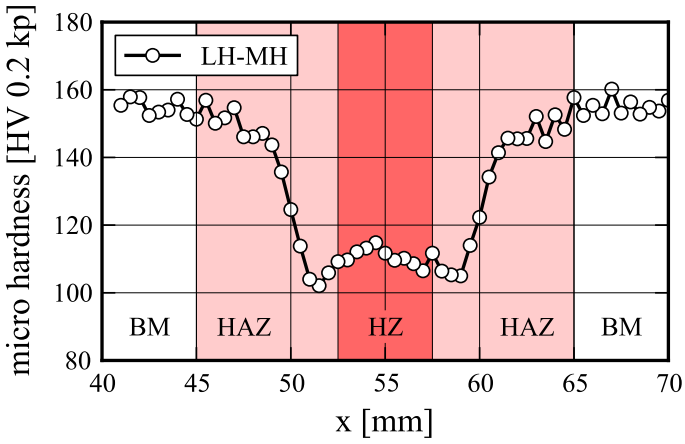

(b)

Figure 5: (a) Measured micro-hardness area scan for the specimen LH-MH. The black dots indicate the measurement positions. The contours were created using a natural neighbour interpolation. (b) Line scan of the micro hardness for $z = 1.8$ mm. Indicated are the lateral extensions of the heating zone (HZ), the heat affected zone (HAZ) and the remaining area with base material properties (BM).

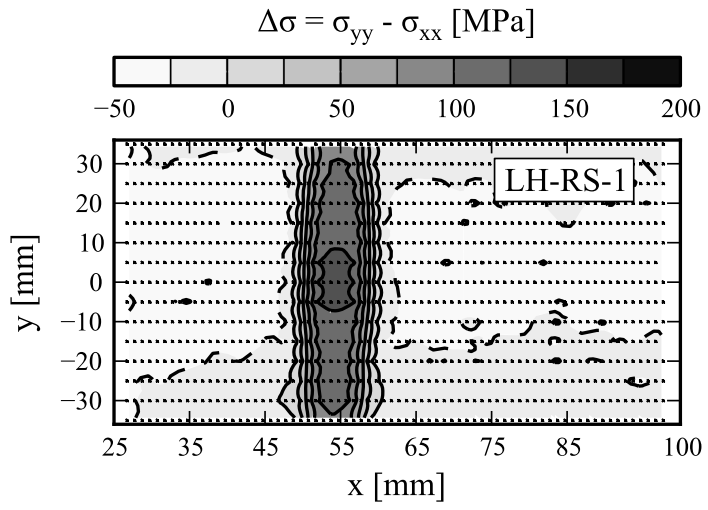

(a)

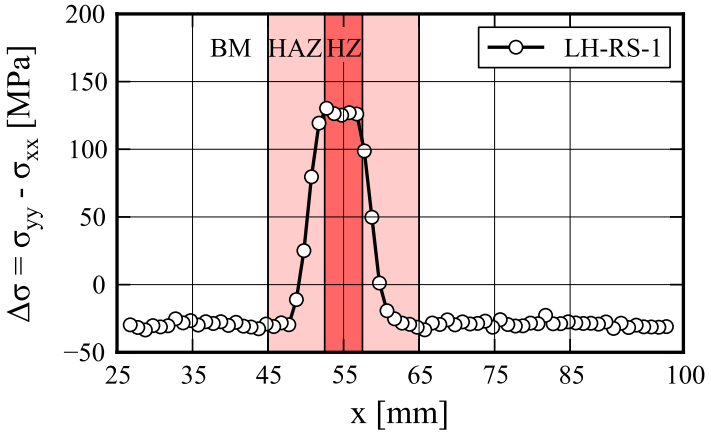

(b)

Figure 6: (a) Measured area scan of the mean stress difference $\Delta\sigma$ for the specimen LH-RS-1. The black dots indicate the measurement positions, and the contours were created using a natural neighbour interpolation. (b) Line scan computed by averaging the area scan data in y direction in the bounds of -12 mm to 12 mm.

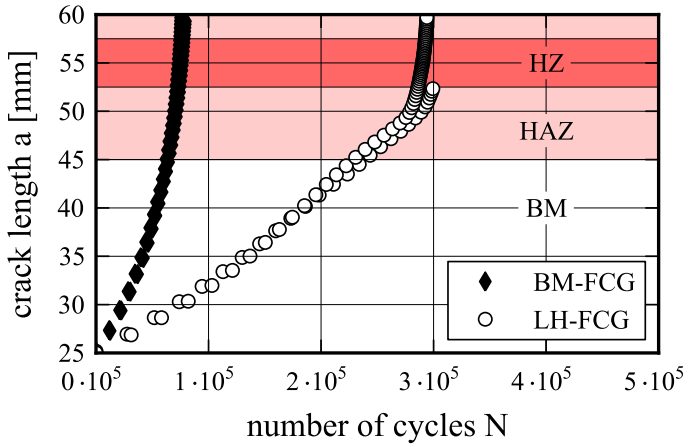

Figure 7: Crack length a as function of the loading cycles N for two base material specimens (BM-FCG-2, BM-FCG-3) and two laser-heated specimens (LH-FCG-2, LH-FCG-3) in T-L orientation. For clarity, only every fifth data point was plotted.

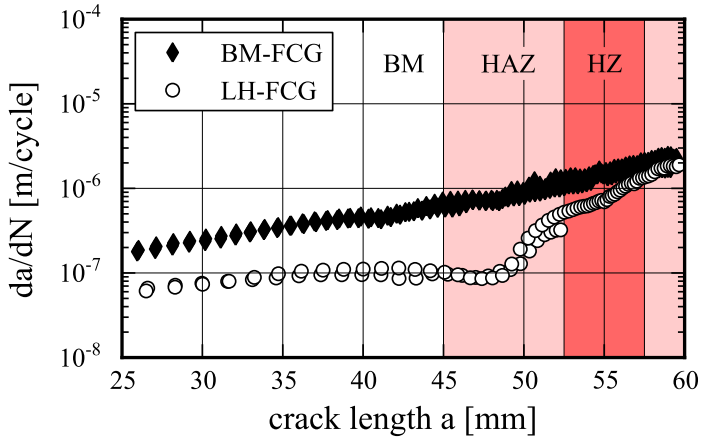

Figure 8: Crack growth rate da/dN as function of the crack length a calculated from the data shown in Fig. 7 for two base material specimens (BM-FCG-2, BM-FCG-3) and two laser-heated specimens (LH-FCG-2, LH-FCG-3) in the T-L orientation. For clarity, only every fifth data point was plotted.